J. Nanostruct Chem. 2026; 16(1): 20-37

Journal of Nanostructure in Chemistry (JNSC)

https://doi.org/10.57647/jnsc.2026.1601.02

Research Article

New forms of Graphitic Carbon Nitride: The Case of S-gC$_3$N$_4$-Au and the Perspectives of a Theragnostic

Jéssica Ingrid Faria de Souza[1], Natália Cristina Gomes da Silva[1], Natália Mayumi Andrade Yoshihara[1], Giulia Sigete[1], Francisco Dheyson de Quadro Carvalho[2], Pedro Hilton Lima Baracho[2], Leticia Nogueira Xavier[2], Lillian Maria Uchôa Dutra Fechine[2], Tiago Melo Freire[2], Luciana Magalhães Rebelo Alencar[3], Alan Silva de Menezes[3], Pierre B. A. Fechine[2], Ralph Santos-Oliveira[1,4*]

[1]*Brazilian Nuclear Energy Commission, Nuclear Engineering Institute, Laboratory of Nanoradiopharmacy and Synthesis of New Radiopharmaceuticals, Rio de Janeiro-RJ, Brazil*
[2]*Group of Chemistry of Advanced Materials (GQMat)- Department of Analytical Chemistry and Physical-Chemistry, Federal University of Ceará, Fortaleza-CE, Brazil*
[3]*Federal University of Maranhão, Department of Physics, Biophysics Laboratory, Campus Bacanga, São Luís-MA,*
[4]*State University of Rio de Janeiro, Laboratory of Nanoradiopharmacy and Strategic Biomaterials, Rio de Janeiro-RJ, Brazil*

[*]**Corresponding authors:** presidenciaradiofarmacia@gmail.com

Article History:

Received:
10 July 2025

Revised:
10 October 2025

Accepted:
27 November 2025

Published in Issue:
28 February 2026

Abstract

This study aimed to develop and characterize a sulfur-doped graphitic carbon nitride (S-g-C$_3$N$_4$) nanosystem functionalized with gold (S-g-C$_3$N$_4$-Au) for potential applications in cancer therapy. The focus was to evaluate its physicochemical properties, cytotoxicity against breast and prostate cancer cells, pharmacokinetics, biodistribution, and biochemical impact in vivo. To carry out the study, S-g-C$_3$N$_4$-Au was synthesized by thermal polymerization of melamine and ammonium sulfate with incorporation of gold seeds. Characterization techniques included SEM, XRD, FTIR, and UV-Vis DRS. Cytotoxicity was evaluated by MTT assays in MDA-MB-231 (breast cancer) and DU-145 (prostate cancer) cell lines. The nanosystem was radiolabeled with technetium-99m for biodistribution and pharmacokinetic studies in Balb/c mice after intraperitoneal administration. Biochemical analyses were conducted to evaluate systemic effects on the liver, kidneys, and metabolic markers. The results obtained demonstrated that the S-g-C$_3$N$_4$-Au nanosystem exhibited a porous, layered morphology with uniformly distributed gold nanoparticles. XRD and FTIR confirmed structural integrity, and SEM, STEM, and EDS confirmed successful gold incorporation. Cytotoxicity assays demonstrated significant, dose-dependent reductions in cell viability in both cancer cell lines, with the effects more pronounced at higher concentrations. In vivo, the nanosystem exhibited predominant accumulation in the liver and small intestine, with low systemic clearance and a plasma elimination half-life of 5.53 hours. Biochemical analysis indicated decreased ALT and glucose levels, but elevated AST, LDH-P, and lipase activities, suggesting stress on liver and digestive tissues. This set of Results demonstrates that the S-g-C$_3$N$_4$-Au nanosystem exhibits favorable physicochemical properties and cytotoxic potential against cancer cells. Its organ-specific biodistribution and prolonged retention highlight its promise for targeted therapy and metabolic modulation. Notably, its ability to be radiolabeled with technetium-99m (99mTc) allows its application in nuclear imaging, further reinforcing its potential as a theranostic platform that integrates diagnostics and therapy in a single nanostructure. However, the observed biochemical alterations reinforce the need for comprehensive toxicological evaluations to ensure safety and enhance therapeutic efficacy.

Keywords: Cytotoxic effect; Cancer cell; Graphite Carbon nitride; 2D g-C$_3$N$_4$

Cite this article: De Souza, J. I. F., Gomes-da-Silva, N. C., Yoshihara, N. M. A., Sigete-Lobo, G., Carvalho, F. D. de Q., Baracho, P. H. L., Xavier, L. N., Fechine, L. M. U. D., Freire, T. M., Alencar, L. M. R., Menezes, A. S., Fechine, P. B. A., & Santos-Oliveira, R.., New forms of Graphitic Carbon Nitride: The Case of S-gC$_3$N$_4$-Au and the Perspectives of a Theragnostic. *J Nanostruct Chem* **16**, 20-37 (2026). https://doi.org/10.57647/jnsc.2026.1601.02

Graphical Abstract

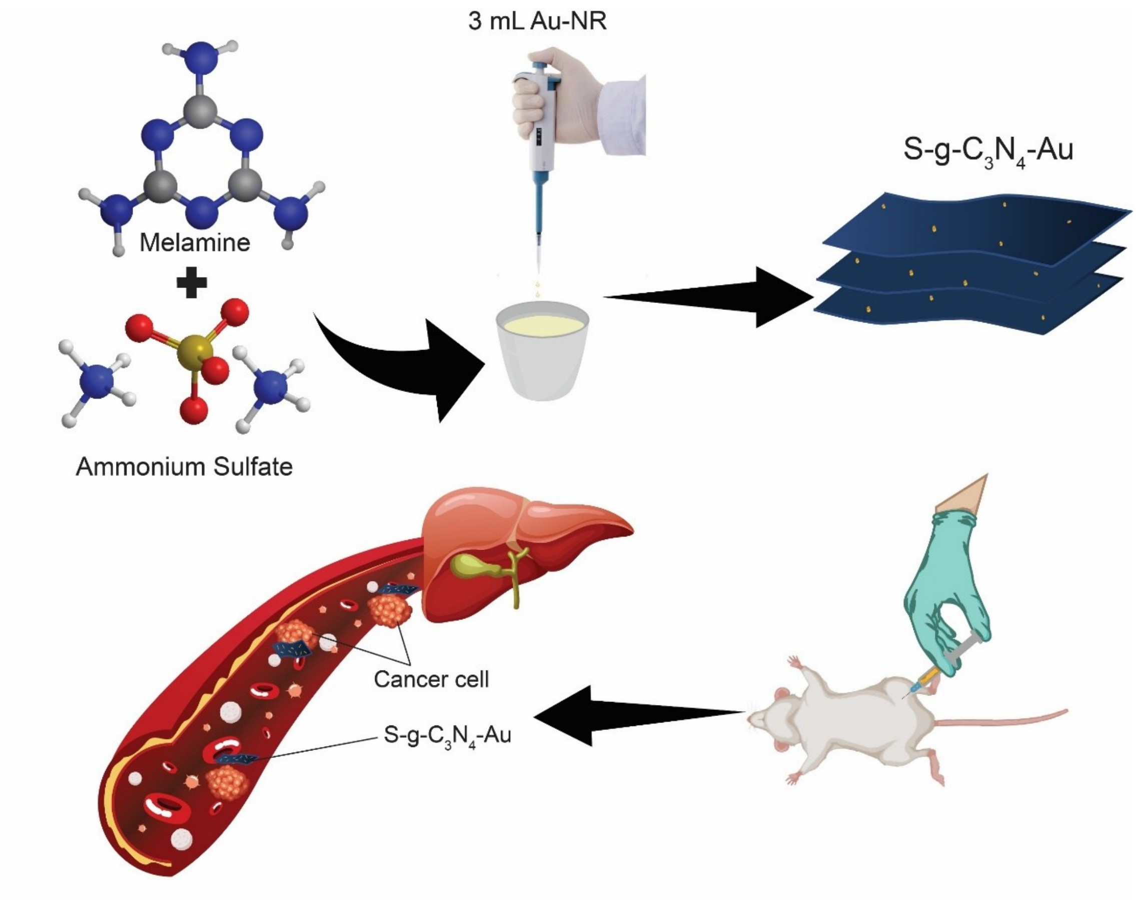

1. Introduction

Breast and prostate cancers remain among the most prevalent and burdensome malignancies worldwide, posing significant challenges in diagnosis, treatment, and long-term management. Breast cancer is the leading cause of cancer-related morbidity among women, while prostate cancer ranks second among men. Both diseases are characterized by considerable biological heterogeneity, necessitating multimodal therapeutic strategies encompassing surgery, radiation, chemotherapy, hormone therapy, and targeted interventions. These approaches, while often effective, contribute substantially to the rising cost of oncology care and underscore the pressing need for more efficient and accessible therapeutic alternatives [1–6].

The burden of these cancers extends beyond clinical considerations to encompass profound economic, psychosocial, and systemic dimensions. Treatment-associated morbidities—such as urinary incontinence, sexual dysfunction, lymphedema, and fatigue—compound the overall impact on patients' quality of life and mental health [7–10]. Additionally, disparities in access to early diagnosis and advanced therapies contribute to suboptimal outcomes, particularly in low- and middle-income countries [11–14]. The increasing incidence of breast and prostate cancers, fueled in part by population aging and expanded screening practices, continues to strain healthcare infrastructures and accentuate the demand for innovative, cost-effective, and targeted interventions [15–17]. Recent advances in cancer biology have catalyzed the development of personalized therapies, particularly those leveraging nanotechnology for precise drug delivery and combined therapeutic-diagnostic (theranostic) applications. In this context, graphitic carbon nitride (g-C_3N_4)—a metal-free, two-dimensional polymeric semiconductor composed of tri-s-triazine units—has emerged as a promising nanomaterial due to its tunable bandgap (~2.7 eV), high surface area, chemical stability, biocompatibility, and photochemical activity [18–20].

Surface modification of g-C_3N_4 enables conjugation with targeting ligands, photosensitizers, and metallic nanoparticles, enhancing its applicability in stimuli-responsive drug release systems. For instance, hybrid formulations incorporating gold nanoparticles have shown synergistic enhancement of PDT and PTT upon near-infrared (NIR) irradiation, leading to improved tumor ablation while minimizing systemic toxicity [21]. Of particular interest is g-C_3N_4's potential in nuclear medicine. Its capacity to be radiolabeled with technetium-99m (99mTc), the most widely used clinical radioisotope, allows for integration into single-photon emission computed tomography (SPECT) imaging. This enables real-time monitoring of pharmacokinetics, tumor accumulation, and biodistribution, facilitating image-guided therapy and refined treatment planning. When combined with therapeutic agents, 99mTc-labeled g-C_3N_4 offers a unified platform for both cancer diagnosis and therapy—hallmarks of modern theranostics. In sum, g-C_3N_4-based nanomaterials present a compelling opportunity at the intersection of nanotechnology, oncology, and radiopharmacy. Their multifunctional properties support a new paradigm in cancer treatment: one that prioritizes precision, integration, and adaptability, particularly in the management of complex diseases such as breast and prostate cancers.

2. Materials and methods

2.1. Preparation of the Seed Solution

The seed solution was prepared by adding gold (III) chloride trihydrate ($HAuCl_4$, >99.9%, Sigma-Aldrich) at a concentration of 0.01 M, preparing 25 mL, and a solution of cetyltrimethylammonium bromide (CTAB, $CH_3(CH_2)_{15}N(Br)(CH_3)_3$, >98.0%, Sigma-Aldrich) at a concentration of 0.1 M, preparing 9.75 mL. Next, a freshly prepared, ice-cold sodium borohydride ($NaBH_4$, >98.0%, Sigma-Aldrich) solution at 0.01 M, preparing 0.6 mL, was added to the mixture and stirred with a magnetic stirrer for 2–3 minutes until the solution turned dark brown. The solution was then incubated at room temperature for 2 hours to allow the gold seeds to grow before use.

2.2. Preparation of the Growth Solution

To synthesize the gold (Au-NR), a growth solution was prepared by first adding 9.0 mL of a 0.1 M cetyltrimethylammonium bromide (CTAB, >98.0%, Sigma-Aldrich) solution to a reaction vessel. Subsequently, 0.5 mL of 0.01 M gold(III) chloride trihydrate ($HAuCl_4$, >99.9%, Sigma-Aldrich), 0.1 mL of 0.01 M silver nitrate ($AgNO_3$, >99.0%, Sigma-Aldrich), and 0.2 mL of 1.0 M hydrochloric acid (HCl, 37%, Sigma-Aldrich) were sequentially added under continuous stirring. After complete mixing, 0.08 mL of 0.1 M ascorbic acid ($C_6H_8O_6$, >99.0%, Sigma-Aldrich) was added as a mild reducing agent, which reduced Au^{3+} ions to Au^+, resulting in a colorless solution. Finally, 1.0 mL of the previously prepared gold seed solution was introduced to initiate gold formation. The final mixture was left undisturbed at room temperature overnight, allowing for the anisotropic growth of gold. In this process, the seed solution acts as a structural template, promoting the directional growth and reduction of Au^+ to metallic gold (Au^0), forming nanoparticles. The successful formation of Au nanoparticles was confirmed by UV–Vis absorption spectroscopy (see Supporting Information, Figure S1).

2.3. Synthesis of S-g-C_3N_4-Au

The sulfur-doped graphitic carbon nitride (S-g-C_3N_4) was synthesized using a two-layer method in a porcelain crucible. Initially, 25 g of ammonium sulfate ($(NH_4)_2SO_4$, 99.0%, Sigma-Aldrich) was placed at the bottom of the crucible to form the first layer. Subsequently, 10 g of melamine ($C_3H_6N_6$, 99.0%, Sigma-Aldrich) was carefully added on top to create the second layer without mixing the two powders. To incorporate gold nanoparticles (S-g-C_3N_4-Au), 3 mL of a freshly prepared gold seed solution was evenly dripped over the melamine layer using a micropipette. The crucible was then covered with a lid and subjected to thermal treatment in a muffle furnace at 550 °C for 4 hours, with a heating rate of 10 °C min^{-1}, under static air conditions. After cooling to room temperature, the resulting yellow powder was collected and ground using an agate mortar and pestle to obtain a homogeneous fine powder. The final product was stored in a desiccator until further use.

2.4. Characterization

The surface morphology and microstructural features of the synthesized S-doped g-C_3N_4–Au nanoparticles were examined using a TESCAN Clara FEG BrightBeam column electron microscope (TESCAN ORSAY Holding SA, Brno, Czech Republic) operating at a voltage of 10 kV from Oxford Instruments. A small amount of the powder sample was evenly dispersed onto a clean aluminum SEM stub using conductive carbon tape to ensure firm adhesion. The crystalline structure of g-C_3N_4 was examined by an X-ray powder diffractometer (Xpert Pro MPD, Panalytical) with Bragg–Brentano geometry and copper $K_{\alpha 1}$ radiation ($\lambda = 1.5406$ Å). The diffraction pattern was recorded by scanning angles from 10° to 90° (2θ) in 0.031° steps with 57.6 s per step. Fourier Transform Infrared Spectroscopy (FTIR) analysis was performed using a Perkin Elmer FTIR/NIR Frontier infrared spectrometer in transmittance mode, covering the 4000 to 550 cm^{-1} range. Using in ATR with the ZnSe crystalline surface. UV-vis diffuse reflection spectroscopy (DRS) was obtained on a model Shimadzu UV-2600 with an integrating sphere (ISR-2600 plus), with $BaSO_4$ as the reference sample. Additional SEM analyses were performed by dispersing S–g-C_3N_4–Au in isopropanol, followed by ultrasonication for 15 min. A drop of the suspension was deposited on a clean silicon substrate and air-dried at room temperature. Imaging was carried out using a field-emission scanning electron microscope (FEG-SEM, FEI Helios NanoLab 650) operated at 18 kV accelerating voltage and 0.2 nA beam current.

Both secondary electron (SE) and backscattered electron (BSE) detectors were employed to obtain complementary information on surface topography and compositional contrast. Each micrograph was acquired with a 2048 × 1768-pixel resolution, dwell time of 10 µs per pixel, and working distance of 4–5 mm. All images were processed using ImageJ (NIH, USA) for contrast enhancement and scale calibration only. Scanning Transmission Electron Microscopy (STEM) analyses were performed using a FEI Titan 80–300 microscope operated at 200 kV in scanning transmission mode. The high-angle annular dark-field (HAADF) detector was used to achieve Z-contrast imaging, where intensity scales approximately with Z^2, allowing clear identification of gold nanodomains against the light C/N background. The convergence semi-angle was 21 mrad and the collection semi-angle 60–200 mrad. Energy-Dispersive X-ray Spectroscopy (EDS) mapping was conducted using a Super-X silicon drift detector (SDD) system with a live time of 60 s per pixel map and a spatial sampling of 512 × 512 pixels. Elemental maps for C, N, O, S, Au, Na, Cl, and Si were collected and processed using Velox software (Thermo Fisher Scientific). The EDS results were treated qualitatively, serving to confirm the spatial co-localization of elements rather than absolute quantification.

2.5. In vitro

2.5.1. *Cell Culture*

2.5.1.1. *Breast Cancer*

MDA-MB-231 human breast cancer cell lines were obtained from the American Type Culture Collection (ATCC HTB-26) and maintained in high-glucose DMEM (Dulbecco's Modified Eagle's Medium) medium supplemented with 10% (v/v) fetal bovine serum, 2 mM L-glutamine, and 1% (v/v) penicillin/streptomycin. The cells were grown and expanded into T75 cm^2 flask bottles and kept in a humidified oven at 5% CO^2 and 37°C.Monolayer assays were performed in 96-well flat-bottom plates.

2.5.1.2. *Prostate Cancer*

Human prostate cancer cell lines (DU-145) were obtained from Cell Bank of Rio de Janeiro (Rio de Janeiro, Brazil). The cells were routinely maintained in RPMI supplemented with 10% FBS, $NaHCO_3$ (2.0 g/L), 4-(2-hydroxyethyl)-1-piperazineethanesulfonic acid (HEPES) (25mM), and 1% penicillin/streptomycin. Cells were incubated at 37 °C in a humidified atmosphere of 5% CO2. Cells were grown to confluence in culture flasks. Cells were detached by brief treatment with trypsin (0.1%)/ ethylenediaminetetraacetic acid (EDTA) (0.01%).

2.6. Treatment with S-g-C_3N_4-Au

After the incubation time, breast and prostate cancer cells, respectively, were cultured in 96-well plates at a concentration of 1 x 10^4 cells. After adhesion for 24 hours, they were treated with concentrations of 10, 25, 50, and 100 µg/ml of S- S-graphitic carbon nitride coated with gold nanoparticles (S-g-C_3N_4-Au) and incubated for 24 hours. A positive death control was performed using the corresponding medium of each cell with 10% (v/v) Triton®. The negative control corresponds to untreated cells grown only in cell culture medium.

2.7. Cell Viability Assay

To assess cytotoxicity in prostate and breast tumor cell lines, we performed the MTT assay, based on Singh et al., 2015 [22]. At the end of the designated time, MTT solution (Sigma) has been added at a 1 mg/ml concentration in the culture and incubated for 2 hours. After the incubation period, formazan crystals were dissolved with DMSO, and absorbance was measured by a multiplate spectrophotometer (Multiskan FC; Thermo Fisher Scientific Inc., Waltham, MA, USA) at a wavelength of 450 nm.

2.8. Animal Experimentation

All procedures were performed in accordance with the Health Guide for the Care and Use of Experimental Animals (CEUA) and approved by the Rio de Janeiro State University Committee (protocol 8059100220/2021), which is in line with the NIH Guidelines for the Care and Use of Laboratory Animals. The experiments were carried out on 4–6-week-old balb/c mice, N = 4 (20-30g). The animals were kept on 12h light/dark cycles with food and water available.

2.9. Radiolabeling of the S-g-C_3N_4-Au

The biodistribution and pharmacokinetic tests performed using Technetium 99m (99mTc) radiolabeling were carried out in accordance with Carvalho, F. D. Q et al., (2025) [23]. The compound was radiolabeled with the isotope Technetium 99m (99mTc) reduced with Stannous Chloride (SnCl2) at a concentration of 80mg/ml in a ratio of 1:1 (v/v). The [99mTc] started from an activity of 142.4

mCi/ 5.27 Mbq, and at the end of the reduction, we obtained an activity of 88.9 uCi/3.28 Mbq per animal. To verify the efficiency of the radiolabeling, quality control was also performed on an automated gamma particle counter (Hidex).

2.10. Biodistribution analysis

The mice (N= 4) were injected with 200uL of S-g-C_3N_4-Au radiolabeled with [99mTc], which corresponded to 3ug of the compound per animal. The injection was made via the intraperitoneal cavity, and after 24 hours, the brain, heart, right and left lungs, stomach, spleen, left and right kidneys, large and small intestines, bladder, urine, and blood (cardiac puncture) were analyzed using an automated gamma particle counter (Hidex).

2.11. Pharmacokinetic Analysis

For the pharmacokinetic analysis, the mice (N = 4) received a dose of S-g-C_3N_4-Au radiolabeled with [99mTc] with an activity of 88.9 uCi/3.28 Mbq per animal, administered through the peritoneum. Subsequently, 2 ml of caudal blood was collected every hour at the following points: 0h, 1h, 2h, 3h, 18h, 22h, 23h, and 24h. The blood samples were read on an automated gamma particle counter (Hidex) to quantify the percentage of injected activity per gram of tissue (%IA/g). This methodology enables precise quantification of the distribution and elimination of the compound over time, ensuring the reproducibility of the results. Additionally, calibration controls were performed before each measurement to validate the accuracy of the readings.

2.12. Biochemical analysis

Blood samples were collected by cardiac puncture from healthy mice (control group) and mice treated (intervention group) with S-g-C_3N_4-Au 24 hours after intraperitoneal administration (N = 4 per group). Blood samples (1 mL) were then placed in microtubes containing 0.5 mL of the anticoagulant heparin (Sigma-Aldrich, Brazil). The plasma was separated by centrifugation (5000 rpm, 5 min, 4 ◦C) and the samples were processed according to the manufacturer's instructions (Bioclin, MG, Brazil) to determine the enzymatic activities, similarly Lee, J. H., et al., (2018) [24], of alanine aminotransferase (ALT), aspartate aminotransferase (AST), gamma GT (GGT), lactate dehydrogenase pyruvate (LDH-P), cholesterol (CHOL), lipase D (LPS), glucose (GLU) and alpha amylase (AMS).

2.13. Statistical analyses

In vitro and *in vivo* experiments, values are expressed as means ± SD. Differences between groups were tested for significance by one-way ANOVA followed by Tukey multiple comparison tests using GraphPad Prism 8.1 software. A *p-value* of ≤ 0.05 was considered significant.

3. Results

3.1. Synthesis of S-g-C_3N_4-Au

The sulfur-doped g-C_3N_4 incorporated with gold nanoparticles was synthesized through the thermal polymerization of melamine and ammonium sulfate, with the addition of a gold seed solution during the synthesis, as shown in Figure 1. Initially, the ammonium sulfate undergoes a series of steps, including gas release, followed by addition, condensation, and nucleation reactions in conjunction with melamine. Melamine, in turn, undergoes condensation, forming a melem structure with the release of ammonia in its gaseous form [25, 26]. Based on the composition and volumes used in the synthesis, the theoretical amount of gold incorporated into the S-g-C_3N_4-Au was estimated. The Au seed solution, prepared from $HAuCl_4$ (0.01 M, 25 mL), contained $2.50\times10{-}4$ mol of Au in the stock solution. Considering the total volume of the seed solution (35.35 mL), the 3.00 mL aliquot applied onto the melamine corresponded to $2.12\times10{-}5$ mol of Au, equivalent to 4.18 mg. This value represents a theoretical loading of approximately 0.070 wt% Au in the final solid, assuming complete retention of the metal after calcination.

3.2. Characterization

The SEM images (Figures 2 A–D) of the S-doped g-C_3N_4–Au composite show a material with a layered and crumpled morphology, consistent with the known structure of graphitic carbon nitride (g-C_3N_4).

This wrinkled matrix provides increased surface area, which is advantageous for catalytic and adsorption applications. The incorporation of sulfur into the g-C_3N_4 framework, although not directly visible in the SEM, may lead to subtle structural modifications or defect formation, contributing to increased surface roughness and potential reactivity.

The SEM and STEM images demonstrated the Au nanoparticles dispersed on the S-doped g-C_3N_4 matrix [27]. These features are homogeneously distributed, with no apparent clustering or aggregation, suggesting a high degree of dispersion and strong interaction between Au species and the g-C_3N_4 support.

The structural integrity of the composite remains preserved, with no evidence of collapse or degradation, indicating good mechanical and thermal stability.

Overall, the presence of Au nanoparticles on S-doped g-C_3N_4, combined with the layered and stable morphology, suggests a multifunctional hybrid material capable of enhanced light absorption, improved charge separation, and promising performance in catalytic or photothermal applications.

The XRD patterns presented in Figure 3a indicate that both S-g-C_3N_4 and S-g-C_3N_4-Au exhibit crystalline characteristics.

For S-g-C_3N_4, two prominent diffraction peaks are observed at 2θ = 12.78° and 27.54°, corresponding to the (100) and (002) planes, respectively. These values are consistent with the standard reference data for graphitic carbon nitride (JCPDS card no. 87-1526) and literature reports [28]. The (100) reflection is associated with the repetition of tri-s-triazine units, allowing the calculation of the distance between the "holes" in the plane, which is 0.693 nm.

The peak related to the (002) planes represents interlayer stacking, revealing a spacing between the sheets of 0.324 nm [29, 30]. In the S-g-C_3N_4-Au sample, the diffraction peaks appear at 12.82° and 27.65°, showing a slight shift toward higher angles. This indicates a minor decrease in interlayer spacing (from 0.324 to 0.322 nm), which can be attributed to the strong interfacial interaction between Au species and the g-C_3N_4 framework.

Notably, the characteristic peaks of metallic gold were not detected, which is fully consistent with the very low theoretical Au loading (~0.07 wt%) and the high degree of nanoparticle dispersion, placing the signal below the detection limit of the employed XRD setup [30, 31].

For the S–g–C_3N_4 sample, the average crystallite size was calculated to be 10.31 nm, and the corresponding dislocation density was estimated as 9.40×10^{-3} nm^{-2}. In comparison, the S-g-C_3N_4-Au sample exhibited a larger crystallite size (12.15 nm).

It is important to notice that these values represent the average coherence length along the (002) stacking direction (c-axis), i.e., the mean thickness of the layered g-C_3N_4 domains, rather than an overall isotropic particle size. Also, a lower dislocation density was found (6.78×10^{-3} nm^{-2}), which may be attributed to the interaction between gold nanoparticles and the graphitic network. The increase in crystallite size, as estimated from the (002) reflection, suggests thicker stacking domains of g-C_3N_4 layers. Separately, the higher crystallinity index indicates an increased proportion of ordered regions relative to amorphous content. Although both parameters point to improved structural order, crystallite size and crystallinity index are distinct and not directly correlated. It is important to notice that these values represent the average coherence length along the (002) stacking direction (c-axis), i.e., the mean thickness of the layered g-C_3N_4 domains, rather than an overall isotropic particle size.These results were obtained using the Scherrer equation [32] based on the (002) diffraction peak. The dislocation density (δ), which provides insight into the defect concentration in the crystalline lattice, was calculated using the expression:

$$\delta = \frac{1}{D^2}, \qquad (1)$$

where D is the crystallite size in nanometers.

The FTIR spectra, presented in Figure 3b, are alike, indicating that S-g-C_3N_4-Au and S-g-C_3N_4 have very similar chemical structures. The broad bands observed in the range of 3400-3000 cm^{-1} can be attributed to the stretching vibrations of the -NH group bonds, characteristic of g-C_3N_4.

Additionally, the region spanning the range of 1650-1200 cm^{-1} includes stretching bands for C-N and C=N bonds in tri-s-triazine rings, typical of g-C_3N_4. The sharp peak around 806 cm^{-1} is associated with C-N bending in the heterocyclic units present in g-C_3N_4 [29, 33]. Small bands were also detected between 2400 and 2300 cm^{-1}, which may be related to stretching involving the S-N bond [31]. Although the optical and spectroscopic results suggest that sulfur doping enhances charge separation and modifies the band structure of g-C_3N_4, a more detailed discussion regarding the structural incorporation of sulfur is warranted. The synthesis procedure adopted in this study is based on the protocol described by Guo et al. (2020), in which sulfur atoms are introduced through thermal treatment of melamine in the presence of ammonium sulfate. Under these conditions, sulfur incorporation likely occurs via substitutional doping, where sulfur atoms replace nitrogen atoms within the tri-s-triazine framework [29]. In this work, we therefore treat sulfur incorporation as inferred from the $(NH_4)_2SO_4$-assisted synthesis and prior reports, rather than directly confirmed by spectroscopy, as noted below.To investigate the optical properties of the materials studied, UV-Vis analysis by diffuse reflectance (DRS) was conducted.

Figure 3c displays the absorbance spectra obtained through reflectance conversion using the Kubelka-Munk equation, showing that the absorption edge for both materials occurred at 440 nm. The unchanged absorption edge suggests that Au did not act as a structural dopant and is only deposited on the material's surface [34]. The band gap energy can be determined using the Tauc method, through the linear extrapolation of the $(\alpha h\nu)^2$ graph versus the energy axis (hν). As shown in Figure 3d, the band gap values obtained for S-g-C_3N_4-Au and S-g-C_3N_4 were 3.03 eV and 3.01 eV, respectively. These values indicate that the presence of Au resulted in a band gap increase. Although the absorption edge remained unchanged, the literature reports that surface modification of g-C_3N_4 with metallic nanoparticles and heteroatomic doping, such as sulfur, can induce effects such as red-shift and modulation of the electronic density.

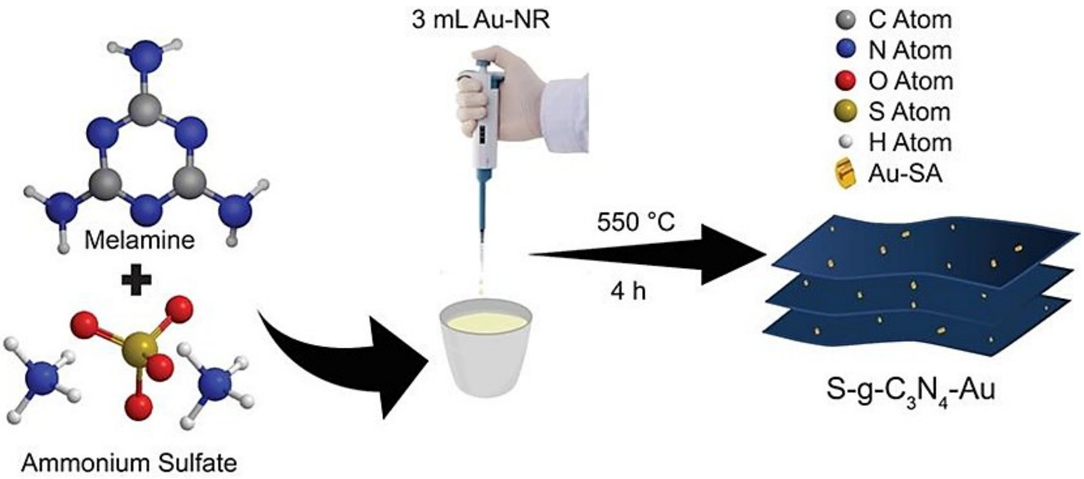

Figure 1. Schematic diagram of the fabrication of S-g-C_3N_4-Au

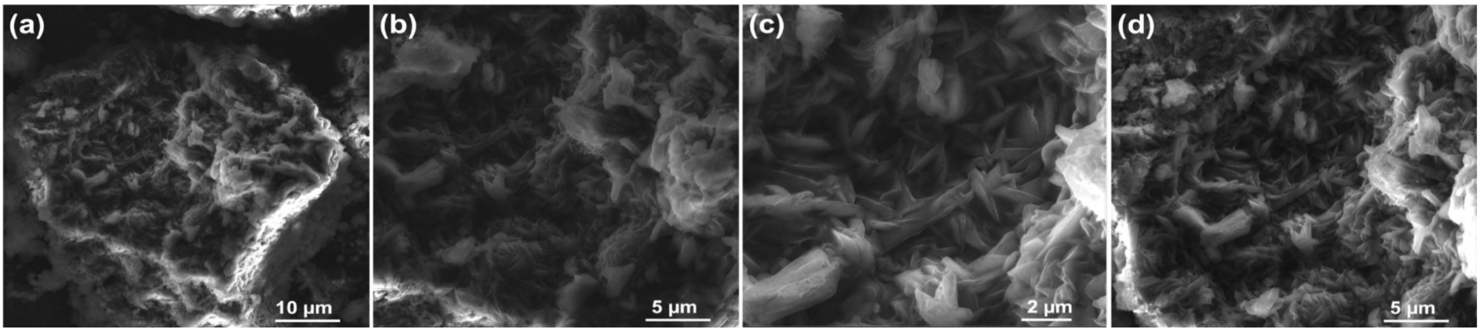

Figure 2. SEM images. (a): Low-magnification SEM image of the S-doped g-C_3N_4–Au composite. The image reveals the general surface morphology of the material, showing the g-C_3N_4 as a layered, wrinkled matrix. Bright contrast points are dispersed across the surface, which may be associated with localized electron-dense regions, possibly corresponding to Au nanoparticles. (b): High-magnification SEM image emphasizing the interaction between Au nanoparticles and the S-doped g-C_3N_4 surface. Although individual atoms are below the spatial resolution of conventional SEM, the observed bright spots suggest dispersed Au species anchored on the substrate, without signs of aggregation. (c): Detailed SEM image of the S-doped g-C_3N_4 nanosheets. The image highlights the characteristic lamellar morphology with increased surface roughness, potentially induced by sulfur doping, which may favor anchoring of metal atoms. (d): SEM image demonstrating the uniform distribution of Au nanoparticles (<5 nm) uniformly dispersed on the S-doped g-C_3N_4 matrix. The absence of visible clusters supports the hypothesis of Au dispersion, which is beneficial for enhancing interfacial charge transfer and catalytic activity.

These changes are frequently associated with the introduction of intermediate states within the bandgap or near the conduction and valence band edges, resulting from the presence of non-metal dopants [35]. Is important to notice that the UV–Vis diffuse reflectance spectra of S-g-C_3N_4-Au and S–g-C_3N_4 composites revealed absorption edges consistent with band-gap energies of approximately 3.03 eV and 3.01 eV, respectively.

Given the negligible difference between these values, we conclude that Au incorporation does not significantly alter the fundamental band gap of S-doped g-C_3N_4. Instead, the main influence of Au is likely associated with changes in charge separation and defect-related states rather than a rigid shift in optical band-gap energy.

The structural and compositional features of the S-doped g-C_3N_4–Au nanohybrid were examined using a suite of electron microscopy techniques, including scanning electron microscopy (SEM), scanning transmission electron microscopy (STEM), and energy-dispersive X-ray spectroscopy (EDS). These complementary modalities enabled a comprehensive multiscale evaluation of the material's morphology, particle dispersion, and elemental distribution. The SEM micrographs (Figure 4a–b) revealed that the S-doped g-C_3N_4–Au exhibits a wrinkled and multilayered morphology, typical of polymeric carbon nitride-based nanostructures.

The crumpled nanosheet topology is beneficial for increasing surface area, enhancing catalytic site availability, and facilitating nanoparticle anchoring.

Discrete bright contrast features, distributed across the matrix, are attributed to gold nanostructures.

The absence of large agglomerates indicates that the Au nanoparticles (NPs) are finely dispersed, likely due to the in-situ seeding process performed before thermal condensation.

Such dispersion is essential to maximize interfacial interactions and optimize plasmonic or catalytic responses. High-angle annular dark-field (HAADF) STEM imaging was employed to achieve Z-contrast imaging, wherein the intensity scales with the atomic number (Z^2).

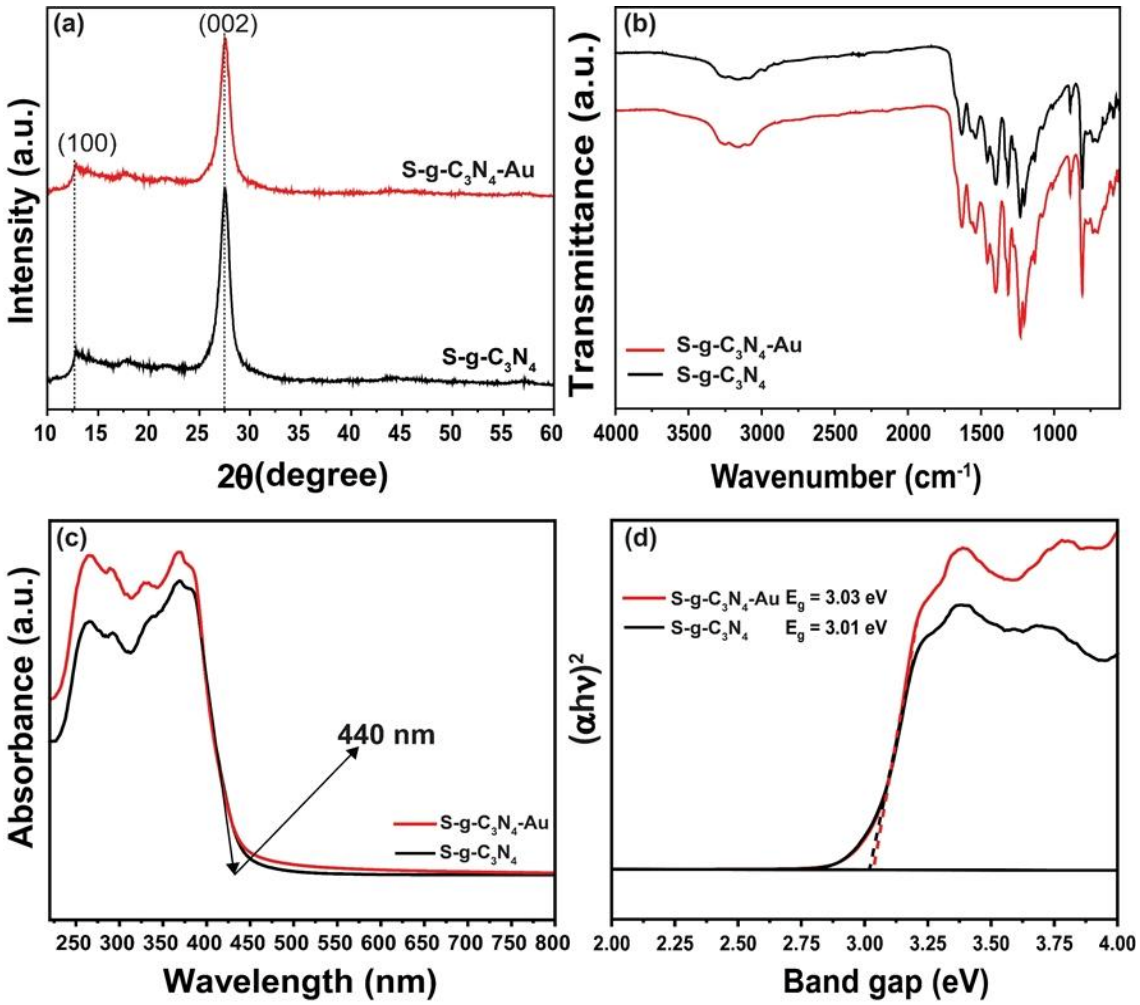

Figure 3. (a) XRD pattern obtained for the synthesis of S-g-C_3N_4-Au and S-g-C_3N_4. (b) Comparative FTIR spectra of S-g-C_3N_4-Au and S-g-C_3N_4. (c) UV–vis diffuse reflectance spectra of S-g-C_3N_4-Au and S-g-C_3N_4. (d) The right is the Kubelka–Munk transformed reflectance spectra and the estimated optical bandgap

In this context, gold (Z = 79) appears significantly brighter than the underlying light elements such as carbon (Z = 6) and nitrogen (Z = 7).

The HAADF-STEM images confirmed the presence of nanoscale Au domains, predominantly <5 nm in diameter, anchored on the g-C_3N_4 matrix. The lack of particle agglomeration suggests strong interfacial adhesion, potentially mediated by surface defects or sulfur-induced vacancy sites within the g-C_3N_4 framework, which are known to act as coordination centers for noble metals. The EDS elemental mapping (Figure 4c) qualitatively confirmed the presence and homogeneous spatial distribution of gold, carbon, and nitrogen within the S-doped g-C_3N_4 matrix.

The Au signal appeared as discrete, localized domains that coincide with the bright regions observed in the HAADF-STEM images, corroborating the presence of finely dispersed Au nanoparticles (<5 nm) anchored on the g-C_3N_4 surface. Given the extremely low theoretical Au loading (≈ 0.07 wt%), quantitative EDS analysis is unreliable, and only a qualitative assessment was performed to verify the spatial correlation between Au and the carbon nitride network. Sulfur was not detected in the EDS spectrum, which is consistent with its expected ultra-low doping level and the intrinsic detection limits of EDS for light elements within a C/N matrix. Substitutional S atoms in g-C_3N_4 typically occur at atomic concentrations below 0.1 at%, well below the sensitivity threshold of conventional EDS systems.

Therefore, the absence of an S signal does not preclude successful doping but rather reflects instrumental constraints. The incorporation of sulfur is thus inferred from the synthesis route involving $(NH_4)_2SO_4$ and supported by prior literature reporting similar substitutional doping under equivalent conditions, which can lead to local lattice distortion and bandgap modulation without direct spectroscopic detection. This interpretation is consistent with both the synthesis stoichiometry and the absence of distinct Au peaks in the XRD results, supporting the formation of a well-dispersed S-g-C_3N_4-Au hybrid material.

The synergistic integration of Au nanostructures with a sulfur-doped g-C_3N_4 matrix yields a hybrid nanomaterial with a high density of interfacial active sites.

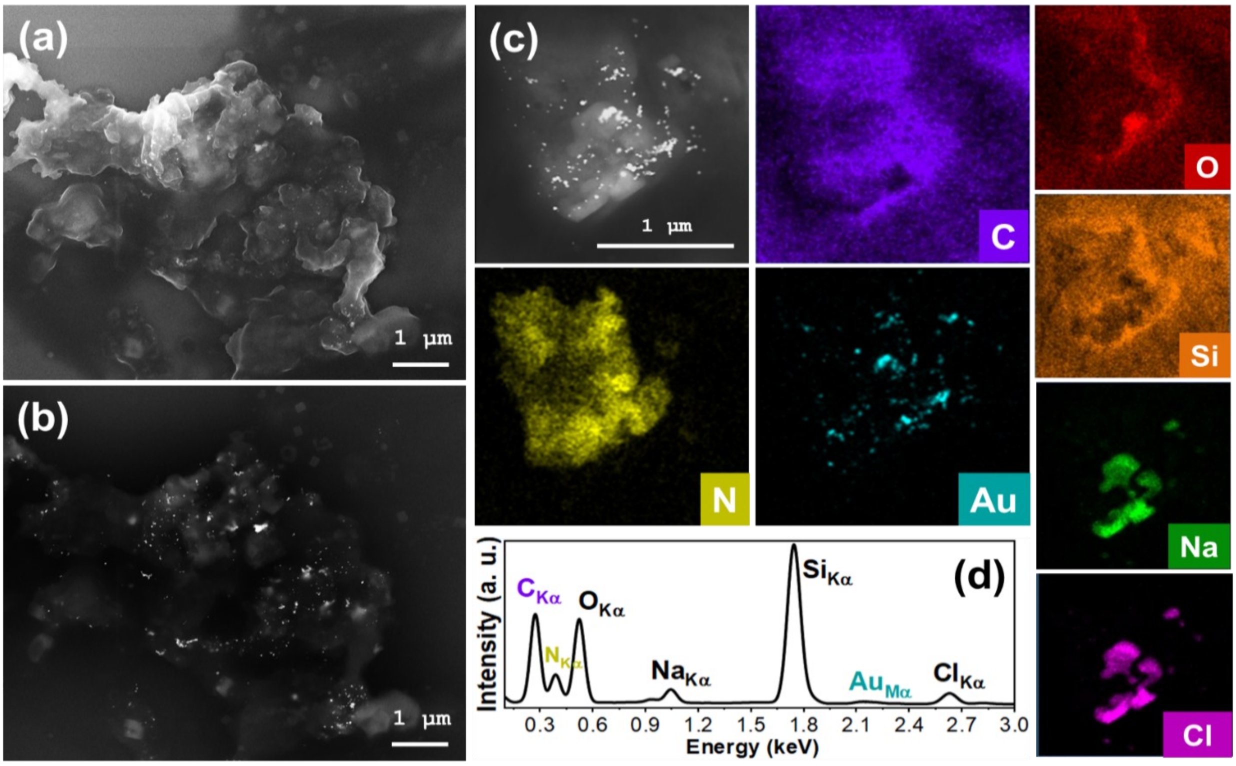

Figure 4. Morphological and compositional characterization of S-doped g-C_3N_4–Au nanostructures. (a) SEM micrograph showing the aggregated and sheet-like morphology of the S-doped g-C_3N_4 framework. (b) Higher magnification SEM image highlighting the dispersion of bright contrast spots corresponding to Au nanostructures deposited on the g-C_3N_4 surface. (c) STEM-EDS elemental mapping of the composite: carbon (C, purple) and nitrogen (N, yellow) signals confirm the g-C_3N_4 matrix; oxygen (O, red) and silicon (Si, orange) likely originate from surface oxidation and residual substrate contributions, respectively. Gold (Au, cyan) is clearly localized as discrete nanoparticles, while sodium (Na, green) and chlorine (Cl, magenta) indicate trace residuals from the synthesis process. (d) Corresponding EDS spectrum of the analyzed region confirming the elemental composition, with characteristic peaks assigned to C, N, O, Na, Si, Au, and Cl

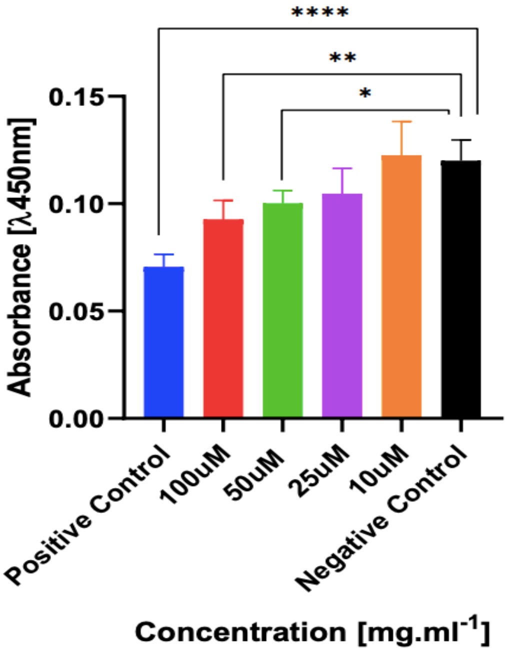

Figure 5. Effects of S-g-C_3N_4-Au-compound on the viability and cell proliferation of breast cancer cell lines (MDA-MD-231). Cell viability was measured after 24 hours of treatment in five different concentrations of S-g-C_3N_4-Au (10, 25, 50 and 100 μg/mL) using an MTT assay. The X-axis shows the absorbance measured at a wavelength of 450 nm. A highly statistically significant difference was observed between the treated and untreated conditions at concentrations of 100 and 50 μg/mL. *$p < 0.05$ was considered significant, **$p < 0.01$ was considered highly significant and ****$p < 0.0001$ was considered highly significant

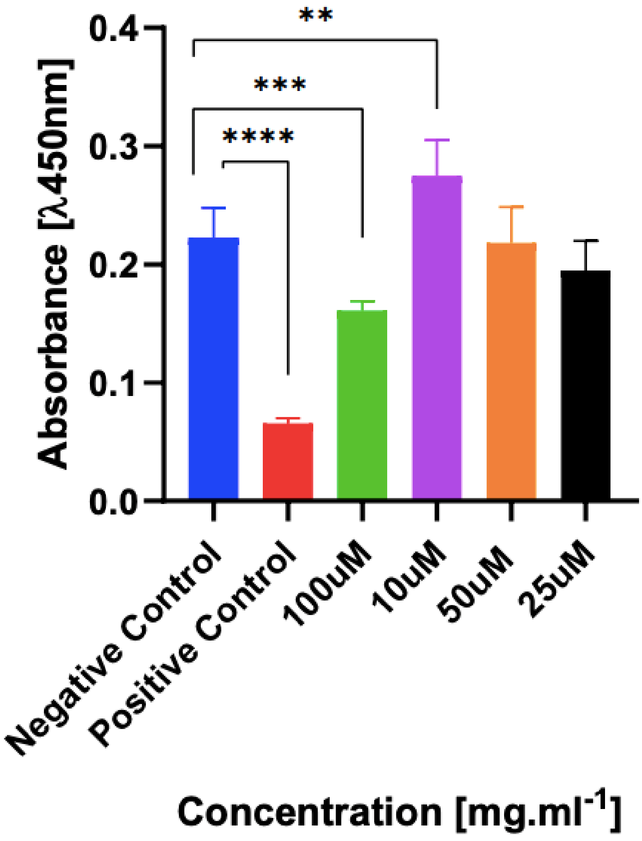

Figure 6. Effects of S-g-C_3N_4-Au compound on the viability and cell proliferation of prostate cancer cell lines (DU-145). Cell viability was measured after 24 hours of treatment in five different concentrations of S-g-C_3N_4-Au (10, 25, 50, and 100 µg/mL) using an MTT assay. The X-axis shows the absorbance measured at a wavelength of 450 nm. A statistically significant difference was observed between the treated and untreated conditions at concentrations of 100 and 10 µg/mL. $*p < 0.05$ was considered significant, $**p < 0.01$ was considered highly significant and $****p < 0.0001$ was considered highly significant

The intimate nanoscale contact between Au and the semiconductor substrate is critical for enhancing charge separation, photothermal conversion, and surface reactivity. The lack of gold nanoparticle aggregation, confirmed across SEM, STEM, and EDS data, reflects not only synthetic precision but also thermal and mechanical stability, which are crucial for downstream biomedical or catalytic applications.

It is important to note that sulfur was not detected in the EDS spectrum (Figure 4). This absence can be attributed to the relatively low concentration of sulfur incorporated into the g-C_3N_4 framework, resulting in signals below the detection threshold of the technique. Moreover, sulfur atoms may substitute nitrogen sites within the lattice, further reducing their spectroscopic visibility. Similar observations have been reported previously, where S-doped g-C_3N_4 exhibited significant electronic modifications despite the lack of a clear sulfur peak in EDS spectra [36–39]. The main role of sulfur doping is to modulate the electronic structure of g-C_3N_4. Sulfur incorporation introduces localized states and narrows the band gap, thereby enhancing visible-light absorption, suppressing electron–hole recombination, and improving charge transfer kinetics. This modification facilitates more efficient migration of photogenerated electrons toward Au nanoparticles, strengthening photocatalytic activity. Although comparative data with non-doped g-C_3N_4 were not included in this study, the beneficial effects of sulfur doping are well established in the literature, particularly in improving photocatalytic hydrogen evolution and pollutant degradation [40, 41].

We acknowledge that confirmatory tests such as Electron Spin Resonance (ESR), radical trapping, and Electrochemical Impedance Spectroscopy (EIS) would provide direct evidence of the electronic effects attributed to sulfur doping. However, these techniques could not be implemented due to instrumental constraints. Our interpretations are therefore based on literature-reported mechanisms under similar synthesis conditions using ammonium sulfate as a sulfur source, where substitutional doping has been established. Future studies are planned to include such advanced characterizations to validate the electronic modulation and charge dynamics hypothesized in this study.

3.3. Cell Viability Assay

There was a significant reduction in tumor cell lines treated with the highest concentrations of S-g-C_3N_4-Au compared to the negative control. For breast cancer tumor cells, the highest concentrations of the compound (100 µM and 50 µM) showed significant results (**$p < 0.01$ and *$p < 0.05$, respectively) when compared to the negative control (Fig. 5). For prostate cancer lines, the highest concentration (100 µg/mL) of graphitic carbon nitride doped with sulfur and coated with gold nanoparticles showed a highly significant difference (****$p < 0.0001$). In addition, there was also a significant difference (**$p < 0.01$) at the lowest concentration of the compound (10 µg/mL) (Fig. 5).

3.4. Biodistribution Assay

The biodistribution study demonstrated a markedly higher uptake of the compound in the liver and small intestine, suggesting these organs as primary sites for the nanosystem accumulation. In contrast, lower uptake levels

This differential uptake pattern suggests that the liver and small intestine may play key roles in the compound's metabolism and excretion, while its reduced presence in other organs could point to lower systemic distribution. Additionally, the lack of significant accumulation in vital organs such as the heart and lungs suggest a targeted organ-specific biodistribution.

3.5. Radiopharmacokinetic analysis

The radiopharmacokinetic analyses (Table 1) were carried out to characterize the absorption, distribution, metabolism, and elimination of radiolabeled S-g-C$_3$N$_4$-Au in healthy mice. It is possible to see that the concentration of the gold-decorated graphitic carbon is preserved in the plasma during the first three hours. In addition, the results of the pharmacokinetic parameters calculated after counting blood samples taken at 1, 2, 3, 18, 22, 23, and 24 h after injection are summarized in Table 1. The values obtained for zero-time concentration, volume of distribution, clearance, and elimination constant were low, while the elimination half-life of the nanosystem solution was reasonably short after intraperitoneal administration in healthy mice.

In these experiments, values are expressed as means ± SD (n = 4). Differences between groups were tested for significance by one-way ANOVA followed by Tukey multiple comparison tests using GraphPad Prism 8.1 software.

3.6. Biochemistry Analysis

The biochemical results of healthy mice treated with the S-gC3N4-Au nanosystem are shown in Table 2 and were observed in the spleen, kidneys, bladder, and large intestine, indicating a more limited distribution in these tissues (Fig. 7).

revealed significant changes. In the control group, ALT averaged 58.93 ± 17.2 U/L, while in the treated group it dropped to 44.2 ± 21.96 U/L. AST levels were low (0.3667 ± 0.2517 U/L) but surged significantly to 37 ± 28.24 U/L after treatment. GGT remained relatively stable, and LDH-P levels increased in the treated group, rising from 290.2 ± 43.52 U/L to 423.4 ± 445.2 U/L. Cholesterol levels dropped dramatically post-treatment, and LPS levels spiked sharply in the treated group. Blood glucose also decreased notably in the treated group.

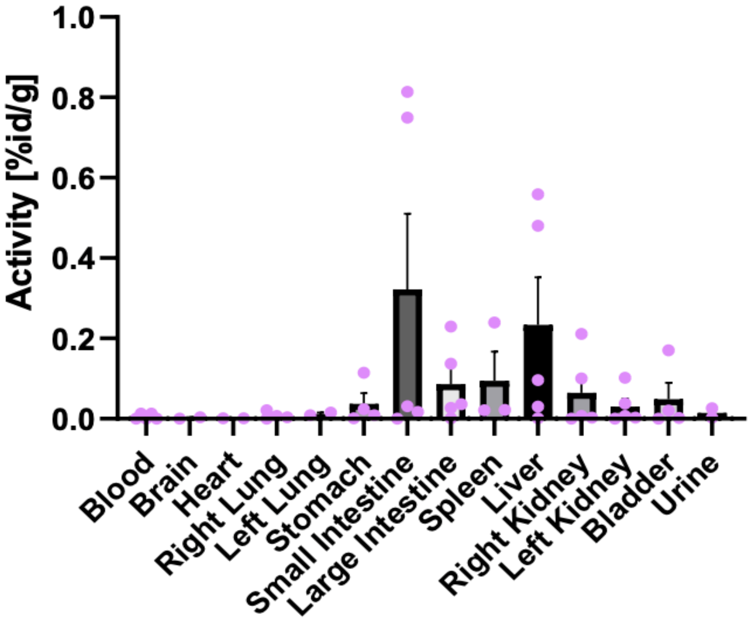

Figure 7. Biodistribution results of S-g-C$_3$N$_4$-Au radiolabeled with [99mTc] in healthy mice 24h after intraperitoneal injection. Graphs show the mean ± SD (n = 4). Data was analyzed by the One-way ANOVA

Table 1. Results of the pharmacokinetic parameters for S-g-C_3N_4-Au radiolabeled with [99mTc] in healthy mice 24h after intraperitoneal injection

Pharmacokinetic parameters	Results 1 – 24h
Concentration at zero-time (co) mg/ml	$6.041 \times 10^{-10} \pm 2.421 \times 10^{-11}$
Elimination rate/elimination constant (k) mg/hour	0.1254 ± 0.005409
Volume of distribution ml	27.98 ± 1.159
Elimination half-life (1/2) days	0.2306 ± 0.01031
Clearance l/hour	$0.3503 \quad .577 \times 10^{-005}$

Table 2. Results of biochemical analysis of blood plasma. *The results marked with an asterisk are derived from data in the literature [42]

	Average ± SD Non-Treated	Average ± SD 24h
ALT (U/L)	58.93 ± 17.2	44.2 ± 21.96
AST (U/L)	0.3667 ± 0.2517	37 ± 28.24
GGT (U/L)	15.1 ± 16.67	14.5 ± 1.229
LDH-P (mg/L)	290.2 ± 43.52	423.4 ± 445.2
CHOL (mg/dL)	95.1 ± 20.02	26 ± 31.09
LPS (mg/L)	2.400 ± 2455	1.869.032 ± 81.394
GLU (mg/dL)	111.2 ± 17.13	30.23 ± 8.391
AMS (U/L)	765.07 ± 132.27*	89.5± 77.63

AMS was not analyzed in the control group; instead, reference values from healthy mice in the literature (765.07 ± 132.27 U/L) were used as a baseline. After treatment, AMS levels decreased to 89.5 ± 77.63 U/L, remaining below the normal range for this enzyme.

These findings highlight that the gold and sulfur-doped graphitic carbon nanosystem led to marked alterations in several enzymes and biomarkers, indicating significant physiological and biochemical effects after 24 hours of exposure. Statistical analysis was performed using ANOVA followed by Tukey's multiple comparison test. The results indicated significant differences ($p < 0.05$) in ALT, AST, LDH-P, and lipase levels, reinforcing the robustness of the observations. Data are presented as mean ± standard deviation ($n = 4$), and all analyses were conducted using GraphPad Prism 8.1 software.

4. Discussion

Previous data have shown that graphitic carbon loaded with metals can be an important tool in the treatment of tumor progression, including prostate cancer and breast cancer [43, 44]. The action of these metals carried by graphitic carbon impacts on DNA replication and prevents cell proliferation of tumor cell lines, which is promising data for the field of anti-tumor therapy [45]. The complexes formed by joining graphitic carbon with gold nanoparticles have already proved effective in treating tumor progression [46,47].

Their various pharmacological and biochemical characteristics, such as toxicity, reactivity, and resistance, are able to leverage the compound's binding to the DNA of tumor cells, penetrating cancerous structures and disrupting them [48–50]. While the S-g-C_3N_4-Au nanosystem shows promising cytotoxicity and favorable biodistribution, its therapeutic potential remains speculative.

The current findings highlight systemic interactions but lack direct *in vivo*. Our biodistribution assay revealed a predominant accumulation of the compound in the liver and small intestine, which stood out significantly when compared to other organs.

This selective uptake suggests that the liver, known for its role in the reticuloendothelial system (RES), acts as a primary site for nanoparticle deposition due to its filtering capacity and phagocytic activity by Kupffer cells [51–54]. These cells are responsible for the efficient capture and processing of nanoparticles, contributing to the high retention observed in this organ. In addition, nanoparticles can be metabolized by liver enzymes, such as cytochrome P450, which participate in the biotransformation of foreign substances [55–58].

The small intestine, with its permeable mucosa and transport proteins, further facilitates the absorption of the compound, likely through mechanisms involving specialized epithelial transporters. Nanoparticles can also interact with intestinal cells and be transported to the lymphatic system, contributing to their higher concentration in these organs.

These metabolic pathways explain the marked deposition observed in these organs. In contrast, while the spleen, kidneys, bladder, and large intestine also demonstrated detectable levels of uptake, their concentrations were notably lower.

The spleen, being another RES organ, likely contributes to particle capture, but its efficiency in this context may be secondary to the liver. The kidneys, which play a key role in the excretion and filtration of smaller compounds, showed lower uptake levels, possibly indicating that the nanoparticles in question are larger or that they are processed by other metabolic pathways before reaching the kidneys [59–62].

The bladder, as part of the urinary excretion pathway, likely reflects the endpoint of renal filtration, while the large intestine might suggest minimal systemic absorption or nanoparticle interaction via the gastrointestinal route [59, 63–67].

This organ-specific distribution highlights the role of the liver and small intestine as major players in the metabolic processing and clearance of this compound. The lower accumulation in the other organs suggests that they participate in the distribution process but to a lesser extent, perhaps due to differences in tissue permeability, organ-specific functions, or nanoparticle characteristics [54, 68].

Together, these results provide a comprehensive understanding of how the compound is distributed across various tissues, emphasizing the hepatic and digestive systems as key pathways in its biodistribution. The high concentration of the graphitic carbon nanosystem in blood plasma in the first 3 hours can be attributed to its initial interaction with plasma proteins and its transient stability in the circulatory system. The gold and sulphur in the nanosystem can form complexes that inhibit immediate phagocytosis and allow prolonged circulation before capture by the reticuloendothelial system [59, 60].

However, after 18 hours, a drastic drop in concentration can occur due to metabolism and progressive elimination. The nanoparticles can be slowly captured by the liver and spleen, where they are processed by enzymes such as proteases and macrophage activity. These enzymes can degrade or modify the nanosystem, facilitating its removal from the plasma [55, 69].

In addition, metabolic pathways involving the reticuloendothelial system contribute to the absorption and elimination of nanoparticles, reflecting the rapid decrease in plasma concentration observed after the initial period [54].

The pharmacokinetic parameters evaluated indicate that in the case of the concentration at time zero (C_0), which reflects the amount of the nanosystem present in the plasma immediately after administration, the extremely low value suggests that the nanosystem is rapidly distributed by the tissues or that its presence in the plasma has been reduced due to interaction with plasma proteins or rapid uptake by organs such as the liver and spleen [70, 71]. The elimination constant (0.1254 mg/h ± 0.0054 mg/h) describes the rate of removal of the nanosystem from the body. This value suggests a relatively slow elimination, possibly influenced by organ absorption mechanisms such as the reticuloendothelial system, which may slow down the process [71, 72]. The volume of distribution, approximately 28 mL, indicates that the nanosystem is distributed widely throughout the body, with potential accumulation in specific tissues such as the liver, spleen, and intestine - a typical behavior of nanoparticles, which tend to deposit in areas with high particle capture activity [71, 73].

The elimination half-life of around 5.53 hours reflects the time needed for the concentration of the nanosystem in the plasma to be halved. This relatively short half-life is indicative of moderate elimination, probably mediated by hepatic metabolization or renal excretion, although a significant fraction may be captured by the reticuloendothelial system [54, 74].

Clearance, which measures the efficiency with which the nanosystem is removed from plasma, has a low value, indicating a slow elimination process. This may be related to the retention of the nanosystem in organs such as the liver and spleen, as well as the slow metabolism or excretion of these particles [75–77].

Taken together, these parameters suggest that the S-g-C_3N_4-Au nanosystem is rapidly distributed throughout the tissues after administration, resulting in a low initial plasma concentration. Although elimination occurs moderately, the low clearance indicates slow capture and metabolization, probably by the liver and spleen, which prolongs its stay in the body.

The wide distribution reflects the compound's ability to accumulate in various tissues, especially in organs that filter and capture particles. The biochemical results reveal a series of significant physiological changes that indicate the impact of treatment on various enzymes and biomarkers.

Alanine aminotransferase (ALT) levels, commonly associated with liver function, decreased significantly in the treated group. This may suggest a possible protection or positive impact of the treatment on the hepatic function [17, 78–80]. However, the significant increase in AST (from 0.3667 U/L to 37 U/L) suggests possible stress on muscle or liver tissues.

Aspartate aminotransferase, being less specific to the liver, may reflect generalized damage to cells with mitochondria, which could be related to the impact of treatment on other organs than the liver [79, 80]. Gamma-glutamyltransferase (GGT), an enzyme involved in glutathione metabolism and indicative of oxidative stress, remained relatively stable between the groups, which may suggest that the antioxidant system was not significantly affected by the treatment.

However, the increase in LDH-P (from 290.2 mg/L in the control to 423.4 mg/L in the treated) points to more extensive cell damage, possibly due to cell disruption in response to the treatment. LDH-P is often associated with tissue damage in organs such as the liver, heart, and skeletal muscles, indicating a systemic response [81–83]. One of the most notable changes was the drastic reduction in cholesterol levels.

This may indicate that treatment with the nanosystem directly affected lipid metabolism, potentially improving the mice's lipid profile. This effect could have positive implications, especially if the system is studied in the context of cardiovascular disease. Similarly, the reduction in blood glucose levels (from 111.2 mg/dL to 30.23 mg/dL) suggests a significant hypoglycemic effect, which may be indicative of an improvement in glucose uptake by the tissues or a change in the regulation of insulin levels [84–86].

The extremely high levels of lipase D in the treated group (from 2,400 mg/L in the control to 1,869,032 mg/L) point to an intense change in lipid metabolism, since this enzyme is responsible for breaking down triglycerides and cholesterol esters in the lysosomes.

This strongly suggests that treatment with the nanosystem may have triggered marked inflammation or tissue damage, possibly in the hepatic system, gastrointestinal tract or other organs, corroborating the biodistribution data mentioned above. The decrease in AMS (amylase) in the treated group (89.5 U/L) compared to data from the literature (765.07 U/L) indicates a possible effect on the digestive system, which may be related to the inflammatory response detected by lipase [87–89].

These results indicate that treatment with the S-g-C_3N_4-Au nanosystem has a profound effect on multiple body systems, from liver and muscle function to lipid and glucose metabolism, as well as triggering significant inflammatory responses. The compound may positively affect metabolic markers like cholesterol and glucose, but potential inflammatory and cytotoxic effects require further investigation.

Additional studies are needed to clarify its mechanisms and assess long-term safety and efficacy. The study offers important data on the pharmacokinetics, biodistribution, and biochemical impact of the S-g-C_3N_4-Au nanosystem, but its toxicological assessment remains limited. Biochemical changes suggest organ-specific effects, yet a complete safety profile is lacking. Future studies will include chronic toxicity models, histology, and inflammatory and oxidative stress markers to better determine long-term safety and clinical potential.

5. Conclusion

The sulfur-doped (consistent with S incorporation; S-doping inferred from the synthesis and literature) graphitic carbon nitride nanosystem incorporating gold nanoparticles (S-g-C_3N_4-Au) demonstrates well-defined crystallinity and favorable structural integration of gold, as evidenced by XRD and spectroscopic analyses. Morphological investigations by SEM revealed a sheet-like, aggregated g-C_3N_4 framework decorated with bright contrast regions corresponding to Au species.

STEM–EDS mapping further confirmed the homogeneous distribution of C and N within the g-C_3N_4 matrix, while Au was localized in discrete regions, validating its successful incorporation.

The detection of residual O, Na, Cl, and Si was attributed to surface oxidation, precursor traces, and substrate contributions. EDS data were used qualitatively (elemental maps/line profiles) owing to the very low S/Au loadings and thin, light-element flakes; no standard-based quantification was performed.

As a perspective, the effective evidence of S-doping would be accessed by XPS (S 2p), CHNS, and/or ToF-SIMS experiments. Collectively, these results highlight the successful synthesis of a structurally stable S-g-C_3N_4-Au system, where gold nanoparticles are effectively anchored onto the g-C_3N_4 support, providing a promising platform for enhanced photocatalytic and electronic applications.

The nanosystem exhibits preferential biodistribution to the liver and small intestine, suggesting organ-specific accumulation and metabolic processing pathways, likely mediated by reticuloendothelial uptake and enzymatic degradation. Pharmacokinetic data reveal rapid systemic distribution and prolonged retention, particularly in clearance-related tissues, underscoring its potential for sustained therapeutic engagement.

Biochemical analyses indicate a dualistic biological impact: on one hand, improvements in metabolic markers such as reduced cholesterol and glucose suggest a modulatory effect on lipid and carbohydrate metabolism; on the other hand, elevations in lipase, amylase, and LDH-P raise concerns about subclinical inflammation and tissue stress, particularly within hepatic and digestive systems. These findings highlight the importance of comprehensive toxicological profiling before translational application. Importantly, the nanosystem’s demonstrated ability to be radiolabeled with technetium-99m (^{99m}Tc) establishes its viability as a theranostic agent, enabling real-time tracking of biodistribution alongside its therapeutic function.

This capability positions S-g-C_3N_4-Au as a promising multifunctional platform for integrated cancer diagnosis and treatment.

However, challenges remain, including the need for long-term toxicity evaluation, confirmation of therapeutic efficacy, and more accurate biodistribution tracking through nuclear imaging. Future investigations should focus on refining targeting strategies, optimizing radiolabeling efficiency, and assessing biocompatibility to fully realize its clinical potential, both in induced animal models and eventual human applications.

Authors Contributions

All authors contributed to the study conception and design. Material preparation, data collection, and analysis were performed by Jéssica Ingrid Faria de Souza, Natália Cristina Gomes da Silva, Mayumi Andrade Yoshihara, Giulia Sigete, Francisco Dheyson de Quadro Carvalho, Pedro Hilton Lima Baracho, Leticia Nogueira Xavier, Lillian Maria Uchôa Dutra Fechine, and Tiago Melo Freire, Diego Wiechers, and Braulio S. Archanjo first draft of the manuscript was written by Luciana Magalhães Rebelo Alencar, Alan Silva de Menezes, Pierre B. A. Fechine, and Ralph Santos-Oliveira. All authors reviewed and commented on previous versions of the manuscript. All authors read and approved the final manuscript.

Funding

This study was funded by Carlos Chagas Filho Foundation for Research Support of Rio de Janeiro State (FAPERJ) (Cientista do Nosso Estado: E-26/200.815/2021; Rede NanoSaude: E-26/010.000981/2019, Pesquisa na UEZO: E-26/010.002362/2019; Temáticos: E-26/211.269/2021, Infraestrutura e Pesquisa na UEZO e UERJ: E-26//211.207/2021, Bolsa de Pós-doutorado Senior (PDS): E-26/202.320/2021) and CNPq (Bolsa de Produtividade 1B: 301069/2018-2) to Ralph Santos-Oliveira, (Bolsa de Produtividade 2: 304774/2021-9) to Luciana Alencar, Universal (401692/2023-0), Internacional (440852/2023-4 and CNPq/Ministerio da Saude -Medicina de Precisão (444089/2023). Finally, this study was supported by Brazilian and Chilean agencies: CNPq (308452/2022–4), CAPES (Finance Code 001—PROEX 23038.000509/2020–82).

Competing Interest

The authors state that they have no conflict of interest.

Availability of data and materials

All data will be available under request.

References

[1] De Silva, F., Alcorn, J.: A Tale of Two Cancers: A Current Concise Overview of Breast and Prostate Cancer. *Cancers (Basel)*. **14**, 2954 (2022).

[2] Rebello, R.J., Oing, C., Knudsen, K.E., Loeb, S., Johnson, D.C., Reiter, R.E., Gillessen, S., Van Der Kwast, T., Bristow, R.G.: Prostate cancer. *Nat Rev Dis Primers*. **7**, 9 (2021).

[3] Arnold, M., Morgan, E., Rumgay, H., Mafra, A., Singh, D., Laversanne, M., Vignat, J., Gralow, J.R., Cardoso, F., Siesling, S., Soerjomataram, I.: Current and future burden of breast cancer: Global statistics for 2020 and 2040. *The Breast* **66**, 15–23 (2022).

[4] Rawla, P. Epidemiology of Prostate Cancer. *World J Oncol* **10**, 63–89 (2019).

[5] Debela, D.T., Muzazu, S.G., Heraro, K.D., Ndalama, M.T., Mesele, B.W., Haile, D.C., Kitui, S.K., Manyazewal, T.: New approaches and procedures for cancer treatment: Current perspectives. *SAGE Open Med* **9**, 1–10 (2021).

[6] Kamal, K.M., Covvey, J.R., Dashputre, A., Ghosh, S., Shah, S., Bhosle, M., Zacker, C.:A Systematic Review of the Effect of Cancer Treatment on Work Productivity of Patients and Caregivers. *J Manag Care Spec Pharm* **23**, 136–162 (2017).

[7] Zhang, W., Cao, G., Wu, F., Wang, Y., Liu, Z., Hu, H., Xu, K.: Global Burden of Prostate Cancer and Association with Socioeconomic Status, 1990–2019: A Systematic Analysis from the Global Burden of Disease Study. *J Epidemiol Glob Health* **13**, 407–421 (2023).

[8] Brunckhorst, O., Liszka, J., James, C., Fanshawe, J.B., Hammadeh, M., Thomas, R., Khan, S., Sheriff, M., Ahmed, H.U., Van Hemelrijck, M., Muir, G., Stewart, R., Dasgupta, P., Ahmed, K.: Mental wellbeing and quality of life in prostate cancer (MIND-P): Protocol for a multi-institutional prospective cohort study. *PLoS ONE* **18**, e0284727 (2023).

[9] Houédé, N., Rébillard, X., Bouvet, S., Kabani, S., Fabbro-Peray, P., Trétarre, B., Ménégaux, F.: Impact on quality of life 3 years after diagnosis of prostate cancer patients below 75 at diagnosis: an observational case-control study. *BMC Cancer* **20**, 757 (2020).

[10] Taylor, J.M., Chen, V.E., Miller, R.C., Greenberger, B.A.: The Impact of Prostate Cancer Treatment on Quality of Life: A Narrative Review with a Focus on Randomized Data. *Res Rep Urol* **12**, 533–546 (2020).

[11] Bhati, D., Deogade, M.S., Kanyal, D. Improving Patient Outcomes Through Effective Hospital Administration: A Comprehensive Review. *Cureus* **15**, e47731. (2023).

[12] Elmore, L.W., Greer, S.F., Daniels, E.C., Saxe, C.C., Melner, M.H., Krawiec, G.M., Cance, W.G., Phelps, W.C.: Blueprint for cancer research: Critical gaps and opportunities. *CA Cancer J Clin* **71**, 107–139 (2021).

[13] Lei, Z.-N., Teng, Q.-X., Tian, Q., Chen, W., Xie, Y., Wu, K., Zeng, Q., Zeng, L., Pan, Y., Chen, Z.-S., He, Y.: Signaling pathways and therapeutic interventions in gastric cancer. *Sig Transduct Target Ther* **7**, 358 (2022).

[14] Barrios, C., De Lima Lopes, G., Yusof, M.M., Rubagumya, F., Rutkowski, P., Sengar, M.: Barriers in access to oncology drugs — a global crisis. *Nat Rev Clin Oncol* **20**, 7–15 (2023).

[15] Sunilkumar, M.M., Finni, C.G., Lijimol, A.S., Rajagopal, M.R.: Health-Related Suffering and Palliative Care in Breast Cancer. *Curr Breast Cancer Rep* **13**, 241–246 (2021).

[16] Schaft, N., Dörrie, J., Schuler, G., Schuler-Thurner, B., Sallam, H., Klein, S., Eisenberg, G., Frankenburg, S., Lotem, M., Khatib, A.: The future of affordable cancer immunotherapy. *Front Immunol* **14**, 1248867 (2023).

[17] Mohammadpour, R., Dobrovolskaia, M.A., Cheney, D.L., Greish, K.F., Ghandehari, H.: Subchronic and chronic toxicity evaluation of inorganic nanoparticles for delivery applications. *Adv Drug Deliv Rev* **144**, 112–132 (2019).

[18] Nawaz, A., Taj, M.B., Carabineiro, S.A.C. Graphitic carbon nitride as an efficient carrier for anti-cancer drug systems: A review. *Next Nanotechnology* **6**, 100074 (2024).

[19] Shamim, M., Perveen, M., Nazir, S., Hussnain, M., Mehmood, R., Khan, M.I., Iqbal, J.: DFT study of therapeutic potential of graphitic carbon nitride (g-C3N4) as a new drug delivery system for carboplatin to treat cancer. *J Mol Liq* **331**, 115607 (2021).

[20] Alipournazari, P., Pourmadadi, M., Abdouss, M., Rahdar, A., Pandey, S.: Enhanced delivery of doxorubicin for breast cancer treatment using pH-sensitive starch/PVA/g-C3N4 hydrogel. *Int J Biol Macromol* **265**, 130901 (2024).

[21] Dash, P., Thirumurugan, S., Nataraj, N., Lin, Y.-C., Liu, X., Dhawan, U., Chung, R.-J.: Near-Infrared Driven Gold Nanoparticles-Decorated g-C3N4/SnS2 Heterostructure through Photodynamic and Photothermal Therapy for Cancer Treatment. *Int J Nanomedicine* **19**, 10537–10550 (2024).

[22] S Singh, R., Kesharwani, P., Mehra, N.K., Singh, S., Banerjee, S., Jain, N.K.: Development and characterization of folate anchored Saquinavir entrapped PLGA nanoparticles for anti-tumor activity. *Drug Dev Ind Pharm* **41**, 1888–1901 (2015).

[23] Carvalho, F.D.D.Q., Gomes-da-Silva, N.C., De Souza, J.I.F., Baracho, P.H.L., Freire, T.M., Xavier, L.N., Fechine, L.M.U.D., Batista, B.D.S., Alencar, L.M.R., De Menezes, A.S., Antunes, R.A., Santos-Oliveira, R., Fechine, P.B.A.: Pharmacokinetic analysis of ultrathin g-C_3N_4 nanosheets via acid exfoliation. *Surf Interfaces* **72**, 107223 (2025).

[24] Lee, M.-K., Han, K.-D., Lee, J.-H., Sohn, S.-Y., Jeong, J.-S., Kim, M.-K., Baek, K.-H., Song, K.-H., Kwon, H.-S.:High hemoglobin levels are associated with decreased risk of diabetic retinopathy in Korean type 2 diabetes. *Sci Rep* **8**, 5538 (2018).

[25] Freire, T.M., Sant'Anna, C., Yoshihara, N., Hu, R., Qu, J., Alencar, L.M.R., Oliveira Da Silva De Barros, A., Helal-Neto, E., Fernandes, L.R., Simoes, R.L., Barja-Fidalgo, C., Fechine, P.B.A., Santos-Oliveira, R.: Biomedical application of graphitic carbon nitrides: tissue deposition in vivo, induction of reactive oxygen species (ROS) and cell viability in tumor cells. *Nanotechnology* **32**, 435301 (2021).

[26] Hong, L., Xu, H., Zhu, Y., Li, Z., Bai, B., Ding, G.: Surface Plasmon Resonance Enhanced Hydrogen Evolution from Water with Graphitic Carbon Nitride Photocatalyst. *Catal Lett* **153**, 2296–2307 (2023).

[27] Arushi, Sharma, A., Arora, A., Mehta, N., Kataria, R., Mehta, S.K.: Au nanoparticles decorated graphitic carbon nitride nanosheets as a sensitive and selective fluorescence probe for Fe3+ and dichromate ions in aqueous medium. *Chemosphere* **363**, 142834 (2024).

[28] Chebanenko, M.I., Zakharova, N.V., Lobinsky, A.A., Popkov, V.I.: Ultrasonic-Assisted Exfoliation of Graphitic Carbon Nitride and its Electrocatalytic Performance in Process of Ethanol Reforming. *Semiconductors* **53**, 2072–2077 (2019).

[29] Guo, H., Shu, Z., Chen, D., Tan, Y., Zhou, J., Meng, F., Li, T.: One-step synthesis of S-doped g-C3N4 nanosheets for improved visible-light photocatalytic hydrogen evolution. *Chemical Physics* **533**, 110714 (2020).

[30] Yang, Y., Yan, J., Zhang, Y., Xing, S., Ran, J., Ma, Y., Li, X.: S/P co-doped g-C3N4 with secondary calcination for excellent photocatalytic performance. *Int J Hydrogen Energy* **51**, 962–974 (2024).

[31] Raziq, F., Humayun, M., Ali, A., Wang, T., Khan, A., Fu, Q., Luo, W., Zeng, H., Zheng, Z., Khan, B., Shen, H., Zu, X., Li, S., Qiao, L.: Synthesis of S-Doped porous g-C3N4 by using ionic liquids and subsequently coupled with Au-TiO2 for exceptional cocatalyst-free visible-light catalytic activities. *Appl Catal B* **237**, 1082–1090 (2018).

[32] Holzwarth, U., Gibson, N.: The Scherrer equation versus the "Debye-Scherrer equation." *Nature Nanotech* **6**, 534–534 (2011).

[33] Mohtasham, H., Gholipour, B., Rostamnia, S., Ghiasi-Moaser, A., Farajzadeh, M., Nouruzi, N., Jang, H.W., Varma, R.S., Shokouhimehr, M.:Hydrothermally exfoliated P-doped g-C3N4 decorated with gold nanorods for highly efficient reduction of 4-nitrophenol. *Colloids Surf A Physicochem Eng Asp* **614**, 126187 (2021).

[34] Liang, S., Xia, Y., Zhu, S., Zheng, S., He, Y., Bi, J., Liu, M., Wu, L.: Au and Pt co-loaded g-C3N4 nanosheets for enhanced photocatalytic hydrogen production under visible light irradiation. *Appl Surf Sci* **358**, 304–312 (2015).

[35] Zhu, B., Xia, P., Li, Y., Ho, W., Yu, J.: Fabrication and photocatalytic activity enhanced mechanism of direct Z-scheme g-C 3 N 4 /Ag 2 WO 4 photocatalyst. *Appl Surf Sci* **391**, 175–183 (2017).

[36] Pérez-Torres, A.F., Hernández-Barreto, D.F., Bernal, V., Giraldo, L., Moreno-Piraján, J.C., Da Silva, E.A., Alves, M.D.C.M., Morais, J., Hernandez, Y., Cortés, M.T., Macías, M.A.:Sulfur-Doped g-C_3 N_4 Heterojunctions for Efficient Visible Light Degradation of Methylene Blue. *ACS Omega* **8**, 47821–47834 (2023).

[37] iu, G., Niu, P., Sun, C., Smith, S.C., Chen, Z., Lu, G.Q. (Max), Cheng, H.-M.: Unique Electronic Structure Induced High Photoreactivity of Sulfur-Doped Graphitic C_3 N_4. *J. Am. Chem. Soc* **132**, 11642–11648 (2010).

[38] Lin, Y.-R., Dizon, G.V.C., Yamada, K., Liu, C.-Y., Venault, A., Lin, H.-Y., Yoshida, M., Hu, C.: Sulfur-doped g-C3N4 nanosheets for photocatalysis: Z-scheme water splitting and decreased biofouling. *J Colloid Interface Sci* **567**, 202–212 (2020).

[39] Kadam, A.N., Moniruzzaman, Md., Lee, S.-W. Dual Functional S-Doped g-C3N4 Pinhole Porous Nanosheets for Selective Fluorescence Sensing of Ag+ and Visible-Light Photocatalysis of Dyes. *Molecules* **24**, 450 (2019).

[40] Xiao, X., Wang, Y., Bo, Q., Xu, X., Zhang, D.: One-step preparation of sulfur-doped porous g-C_3 N_4 for enhanced visible light photocatalytic performance. *Dalton Trans* **49**, 8041–8050 (2020).

[41] Guan, K., Li, J., Lei, W., Wang, H., Tong, Z., Jia, Q., Zhang, H., Zhang, S.: Synthesis of sulfur doped g-C3N4 with enhanced photocatalytic activity in molten salt. *J Mater* **7**, 1131–1142 (2021).

[42] Almeida, A.S., Faleiros, A.C.G., Teixeira, D.N.S., Cota, U.A., Chica, J.E.L.: Valores de referência de parâmetros bioquímicos no sangue de duas linhagens de camundongos. *J Bras Patol Med Lab* **44**, 429–432 (2008).

[43] Xu, M., Yang, G., Bi, H., Xu, J., Feng, L., Yang, D., Sun, Q., Gai, S., He, F., Dai, Y., Zhong, C., Yang, P.: Combination of CuS and g-C3N4 QDs on upconversion nanoparticles for targeted photothermal and photodynamic cancer therapy. *Chem Eng J* **360**, 866–878 (2019).

[44] Godwin, M.A., Mahithashri, K., Shiney, O.J., Bhagat, M., Praseetha, P.K.: Metal Incorporated g-C_3 N_4 Nanosheets as Potential Cytotoxic Agents for Promoting Free Radical Scavenging in Cancer Cell Lines. *J Nanosci Nanotechnol* **19**, 5448–5455 (2019).

[45] P Padmanabhan, V.P., Sivashanmugam, P., S. M., M., Sagadevan, S., Kulandaivelu, R.: The development of ZnO nanoparticle-embedded graphitic-carbon nitride towards triple-negative breast cancer therapy. *RSC Adv* **13**, 24333–24342 (2023).

[46] Muhammad, N., Guo, Z. Metal-based anticancer chemotherapeutic agents. *Curr Opin Chem Biol* **19**, 144–153 (2014).

[47] Khan, H.Y., Ansari, M.F., Tabassum, S., Arjmand, F.: A review on the recent advances of interaction studies of anticancer metal-based drugs with therapeutic targets, DNA and RNAs. *Drug Discov Today* **29**, 104055 (2024).

[48] Hannon, M.J. Metal-based anticancer drugs: From a past anchored in platinum chemistry to a post-genomic future of diverse chemistry and biology. *Pure Appl Chem* **79**, 2243–2261 (2007).

[49] Bufarwa, S.M., El-Sefait, R.M., Thbayh, D.K., Belaidi, M., Al-Shemary, R.K., Abdusamea, Rema.M., El-Ajaily, M.M., Fiser, B., Bader, H.A., Saleh, A.A., Bufarwa, M.M.: Antituberculosis, antimicrobial, antioxidant, cytotoxicity and anti-inflammatory activity of Schiff base derived from 2,3-diaminophenazine moiety and its metal(II) complexes: structural elucidation, computational aspects, and biological evaluation. *Rev Inorg Chem* **45**, 105–124 (2025).

[50] Naseem, K., Aziz, A., Khan, M.E., Ali, S., Khalid, A.: Bioinorganic metal nanoparticles and their potential applications as antimicrobial, antioxidant and catalytic agents: a review. *Rev Inorg Chem* **45**, 207–236 (2025).

[51] Duan, X., Li, Y. Physicochemical Characteristics of Nanoparticles Affect Circulation, Biodistribution, Cellular Internalization, and Trafficking. *Small* **9**, 1521–1532 (2013).

[52] Owens, D.E., Peppas, N.A. Opsonization, biodistribution, and pharmacokinetics of polymeric nanoparticles. *Int J Pharm* **307**, 93–102 (2006).

[53] Åslund, A.K.O., Vandebriel, R.J., Caputo, F., De Jong, W.H., Delmaar, C., Hyldbakk, A., Rustique, E., Schmid, R., Snipstad, S., Texier, I., Vernstad, K., Borgos, S.E.F.: A comparative biodistribution study of polymeric and lipid-based nanoparticles. *Drug Deliv and Transl Res* **12**, 2114–2131 (2022).

[54] Kumar, M., Kulkarni, P., Liu, S., Chemuturi, N., Shah, D.K.: Nanoparticle biodistribution coefficients: A quantitative approach for understanding the tissue distribution of nanoparticles. Adv *Drug Deliv Rev* **194**, 114708 (2023).

[55] Liu, T., Choi, H., Zhou, R., Chen, I.-W.: Quantitative Evaluation of the Reticuloendothelial System Function with Dynamic MRI. *PLoS ONE* **9**, e103576 (2014).

[56] Li, S.-D., Huang, L. Nanoparticles evading the reticuloendothelial system: Role of the supported bilayer. *Biochim Biophys Acta Biomembr* **1788**, 2259–2266 (2009).

[57] Tang, Y., Wang, X., Li, J., Nie, Y., Liao, G., Yu, Y., Li, C.: Overcoming the Reticuloendothelial System Barrier to Drug Delivery with a “Don’t-Eat-Us” Strategy. *ACS Nano* **13**, 13015–13026 (2019).

[58] Zhang, M., Gao, S., Yang, D., Fang, Y., Lin, X., Jin, X., Liu, Y., Liu, X., Su, K., Shi, K.: Influencing factors and strategies of enhancing nanoparticles into tumors in vivo. *Acta Pharm Sin B* **11**, 2265–2285 (2021).

[59] Zhang, X.-D., Wu, D., Shen, X., Liu, P.-X., Fan, F.-Y., Fan, S.-J.: In vivo renal clearance, biodistribution, toxicity of gold nanoclusters. *Biomaterials* **33**, 4628–4638 (2012).

[60] Daems, N., Verlinden, B., Van Hoecke, K., Cardinaels, T., Baatout, S., Michiels, C., Lucas, S., Aerts, A.: In Vivo Pharmacokinetics, Biodistribution and Toxicity of Antibody-Conjugated Gold Nanoparticles in Healthy Mice. *J Biomed Nanotechnol* **16**, 985–996 (2020).

[61] Escudero-Francos, M.A., Cepas, V., González-Menédez, P., Badía-Laíño, R., Díaz-García, M.E., Sainz, R.M., Mayo, J.C., Hevia, D.: Cellular Uptake and Tissue Biodistribution of Functionalized Gold Nanoparticles and Nanoclusters. *J Biomed Nanotechnol* **13**, 167–179 (2017)

[62] Li, N., Chen, L., Zeng, C., Yang, H., He, S., Wei, Q.: Comparative Toxicity, Biodistribution and Excretion of Ultra-Small Gold Nanoclusters with Different Emission Wavelengths. *J Biomed Nanotechnol* **17**, 1778–1787 (2021).

[63] Colino, C.I., Lanao, J.M., Gutierrez-Millan, C. Targeting of Hepatic Macrophages by Therapeutic Nanoparticles. *Front. Immunol* **11**, 218 (2020).

[64] De Matteis, V. Exposure to Inorganic Nanoparticles: Routes of Entry, Immune Response, Biodistribution and In Vitro/In Vivo Toxicity Evaluation. *Toxics* **5**, 29 (2017).

[65] Zelepukin, I.V., Shevchenko, K.G., Deyev, S.M. Rediscovery of mononuclear phagocyte system blockade for nanoparticle drug delivery. *Nat Commun* **15**, 4366 (2024).

[66] Gustafson, H.H., Holt-Casper, D., Grainger, D.W., Ghandehari, H.: Nanoparticle uptake: The phagocyte problem. *Nano Today* **10**, 487–510 (2015).

[67] Albanese, A., Tang, P.S., Chan, W.C.W. The Effect of Nanoparticle Size, Shape, and Surface Chemistry on Biological Systems. *Annu Rev Biomed Eng* **14**, 1–16 (2012).

[68] Wei, Y., Quan, L., Zhou, C., Zhan, Q.: Factors Relating to the Biodistribution & Clearance of Nanoparticles & Their Effects on *In Vivo* Application. *Nanomedicine (Lond)* **13**, 1495–1512 (2018).

[69] Tavares, A.J., Poon, W., Zhang, Y.-N., Dai, Q., Besla, R., Ding, D., Ouyang, B., Li, A., Chen, J., Zheng, G., Robbins, C., Chan, W.C.W.:Effect of removing Kupffer cells on nanoparticle tumor delivery. *Proc Natl Acad Sci U S A* **114**, (2017).

[70] Pandey, P., Patel, J., Kumar, S., Pathak, Y.: Pharmacokinetics and Pharmacodynamics of Liposomal Nanoparticles. In: Patel, J.K. and Pathak, Y.V. (eds.) Pharmacokinetics and Pharmacodynamics of Nanoparticulate Drug Delivery Systems. pp. 143–158. Springer International Publishing, Cham (2022).

[71] Verma, A.K., Kumar, A. Pharmacokinetics and biodistribution of negatively charged pectin nanoparticles encapsulating paclitaxel. *Cancer Nano* **4**, 99–102 (2013).

[72] Haripriyaa, M., Suthindhiran, K. Pharmacokinetics of nanoparticles: current knowledge, future directions and its implications in drug delivery. *Futur J Pharm Sci* **9**, 113 (2023).

[73] Li, J., Wang, H. Selective organ targeting nanoparticles: from design to clinical translation. *Nanoscale Horiz* **8**, 1155–1173 (2023).

[74] Y Yoshioka, Y., Higashisaka, K., Tsunoda, S., Tsutsumi, Y.: The Absorption, Distribution, Metabolism, and Excretion Profile of Nanoparticles. In: Akashi, M., Akagi, T., and Matsusaki, M. (eds.) Engineered Cell Manipulation for Biomedical Application. pp. 259–271. Springer Japan, Tokyo. (2014)

[75] Alexis, F., Pridgen, E., Molnar, L.K., Farokhzad, O.C.: Factors Affecting the Clearance and Biodistribution of Polymeric Nanoparticles. *Mol Pharm* **5**, 505–515 (2008).

[76] Wang, L., Quine, S., Frickenstein, A.N., Lee, M., Yang, W., Sheth, V.M., Bourlon, M.D., He, Y., Lyu, S., Garcia-Contreras, L., Zhao, Y.D., Wilhelm, S.: Exploring and Analyzing the Systemic Delivery Barriers for Nanoparticles. *Adv Funct Materials* **34**, 2308446 (2024).

[77] Hu, J., Sheng, Y., Shi, J., Yu, B., Yu, Z., Liao, G.:Long Circulating Polymeric Nanoparticles for Gene/Drug Delivery. *Curr Drug Metab* **19**, 723–738 (2018).

[78] Guyton, A.C., Hall, J.E. *Textbook of medical physiology*. Elsevier Saunders, Philadelphia (2006)

[79] Huang, X.-J., Choi, Y.-K., Im, H.-S., Yarimaga, O., Yoon, E., Kim, H.-S.: Aspartate Aminotransferase (AST/GOT) and Alanine Aminotransferase (ALT/GPT) Detection Techniques. *Sensors* **6**, 756–782 (2006).

[80] Das, S.K., Sen, K., Ghosh, B., Ghosh, N., Sinha, K., Sil, P.C.: Molecular mechanism of nanomaterials induced liver injury: A review. *World J Hepatol* **16**, 566–600 (2024).

[81] Zhang, H., Kang, K., Chen, S., Su, Q., Zhang, W., Zeng, L., Lin, X., Peng, F., Lin, J., Chai, D.: High serum lactate dehydrogenase as a predictor of cardiac insufficiency at follow-up in elderly patients with acute myocardial infarction. *Arch Gerontol Geriatr* **117**, 105253 (2024).

[82] Khan, A.A., Allemailem, K.S., Alhumaydhi, F.A., Gowder, S.J.T., Rahmani, A.H.: The Biochemical and Clinical Perspectives of Lactate Dehydrogenase: An Enzyme of Active Metabolism. Endocr *Metab Immune Disord Drug Targets* **20**, 855–868 (2020).

[83] Rafaqat, S., Radoman Vujacic, I., Behnoush, A.H., Sharif, S., Klisic, A.: Role of Cardiac Biomarkers in Hepatic Disorders: A Literature Review. *Metab Syndr Relat Disord* **22**, 251–262 (2024).

[84] Grundy, S.M., Stone, N.J., Bailey, A.L., Beam, C., Birtcher, K.K., Blumenthal, R.S., Braun, L.T., De Ferranti, S., Faiella-Tommasino, J., Forman, D.E., Goldberg, R., Heidenreich, P.A., Hlatky, M.A., Jones, D.W., Lloyd-Jones, D., Lopez-Pajares, N., Ndumele, C.E., Orringer, C.E., Peralta, C.A., Saseen, J.J., Smith, S.C., Sperling, L., Virani, S.S., Yeboah, J.: 2018 AHA/ACC/AACVPR/AAPA/ABC/ACPM/ADA/AGS/APhA/ASPC/NLA/PCNA Guideline on the Management of Blood Cholesterol: Executive Summary. *J Am Coll Cardiol* **73**, 3168–3209 (2019).

[85] Tong, S., Luo, S., Yang, Q., Song, B., Chang, R., Wu, J.: Preparation and biological evaluation of a glucose-responsive block copolymer nanoparticle with the ability to ameliorate diabetic kidney damage. *Eur Polym J* **220**, 113472 (2024).

[86] Mohammadparast, V., Mallard, B.L. The effect and underlying mechanisms of titanium dioxide nanoparticles on glucose homeostasis: A literature review. *J Appl Toxicol* **43**, 22–31 (2023).

[87] Lin, Q., Qiu, C., Li, X., Sang, S., McClements, D.J., Chen, L., Long, J., Jiao, A., Tian, Y., Jin, Z.:The inhibitory mechanism of amylase inhibitors and research progress in nanoparticle-based inhibitors. *Crit Rev Food Sci Nutr* **63**, 12126–12135 (2023)

[88] Jalal, M., Gbadegesin, S.A., Tehami, N., Nakajima, K.: What is the clinical significance of low serum amylase? Systematic review of the conditions associated with low serum amylase. *Frontline Gastroenterol* **15**, 154–161 (2024).

[89] Ko, J., Cho, J., Petrov, M.S. Low serum amylase, lipase, and trypsin as biomarkers of metabolic disorders: A systematic review and meta-analysis. *Diabetes Res Clin Pract* **159**, 107974 (2020).